Analysis of runaway electron expulsion during tokamak instabilities detected by a single-channel Cherenkov probe in FTU

F. Causa[1], P. Buratti[2] and FTU Team[3]

1 Istituto di Fisica del Plasma 'Piero Caldirola', CNR, Milano, Italy

2 ENEA, Fusion and Nuclear Safety Department, C. R. Frascati, Via E. Fermi 45, I-00044 Frascati (Roma), Italy

3 See the appendix of G. Pucella et al, Proceedings of the 26th IAEA Fusion Energy Conf., Kyoto, Japan, 2016

Abstract

The expulsion of runaway electrons (RE) during different types of tokamak instabilities is analysed by means of a Cherenkov probe inserted in the scrape-off layer of the FTU tokamak. One such instability, the well-known tearing mode, is involved in disruptive plasma termination events, during which the risk of runaway electron avalanche multiplication is highest. The second type, known as anomalous Doppler instability, influences RE dynamics by enhancing pitch angle scattering. Three scenarios are analysed here, characterised by different RE generation rates and mechanisms. The main conclusions are drawn from correlations between the Cherenkov probe and other diagnostics. In particular, the Cherenkov probe permits the detection of fast electrons expulsion with a high level of detail, presenting peaks with 100% signal contrast during tearing mode growth and rotation, and sub-peak structures reflecting the interplay between the magnetic island formed by the tearing mode, runaway electron diffusion during island rotation and the geometry of obstacles in the vessel. Correlations between Cherenkov signal, gamma-ray emission and electron cyclotron emission reveal the impulsive development of the anomalous Doppler instability with instability rise time in the microsecond scale resolved by the high time-resolution of the Cherenkov probe.

1. Introduction

Runaway Electron (RE) beams with multi-MeV energies can develop within a tokamak plasma either at low density, or during disruptive instabilities. REs represent a major concern in tokamaks because when lost to the first wall they can cause significant local energy deposition, melting and damage to plasma-facing components [1]. Key to the successful operation of tokamaks, and in particular of ITER and future energy-generation reactors of the DEMO type, is the understanding of the dynamics of REs to enable efficient control techniques to mitigate their impact on machine operation.

An accurate diagnosis of the dynamics of runaway electrons (REs) lost from tokamak plasmas is essential to understand RE generation and transport mechanisms, and, ultimately, to enable effective control schemes to minimise damage to plasma-facing components. Particularly important in this respect are losses due to instabilities developing during the various phases of tokamak disruptions (precursor, thermal quench, current quench, and possibly RE carried current plateau) [2]. Losses occurring before the current quench determine the number of REs that constitute the seed for avalanche acceleration. Furthermore, the spatial structure of losses in the presence of non-axisymmetric perturbations influences the power density load on plasma-facing components. Enhanced and modulated RE losses have indeed been observed in connection with tearing modes developing magnetic islands [3].

An excellent candidate for the direct detection of fast escaping electrons is the Cherenkov effect because it transforms the problem into an optical one, namely the detection of photons emitted by charged particles travelling through a radiator (in this case, a transparent dielectric). Diagnostics based on such effect are widely used in high-energy physics and astrophysics, [4]; and are beginning now to be utilised also in fusion plasma physics. In particular, in tokamaks, they are presently implemented in the form of fibre-coupled, multi-channel detectors [5].

A single-channel detector implemented on the FTU tokamak, [6], has demonstrated high sensitivity and quantitative correlation with other plasma diagnostics, in particular with electron cyclotron emission (ECE), gamma and neutron detectors, providing evidence of loss of confinement of energetic electrons in a variety of scenarios, with a level of detail providing a deeper insight into the mechanisms of RE losses. In [6] several scenarios were analysed, including tearing modes, BAEs (Beta-induced Alfvèn Eigenmodes), pellet injection and plasma discharge soft stop imposed by high RE levels, leading to the following useful observations. In the presence of magnetic islands, Cherenkov signal maxima occur when the O-point of the island faces the probe, while the signal vanishes when the O-point moves away from the probe. In such cases, RE emission is dominated by island rotation, confirming that one mechanism of RE expulsion is the interaction of fast electrons with the magnetic perturbation due to the island. In the presence of BAEs, a bursty emission modulated by the slow, nearly-locked island rotation frequency was observed, indicating that in such cases island amplitude fluctuations contribute as an additional RE expulsion mechanisms. That observation was substantiated by the presence of high frequency components in the Cherenkov signal, making that the first detection of BAEs in FTU using a non-magnetic plasma diagnostics, [6].

The analysis described in the present paper advances our understanding of the wide-ranging capabilities of the Cherenkov probe in detecting RE losses in different scenarios, thus enabling its exploitation in the prediction and control of disruptions in next-generation tokamaks. Results are

presented from the correlation of the Cherenkov signal with gamma counts and with amplitude and phase of magnetic perturbations, and from the analysis of fast kinetic instabilities detected by the Cherenkov probe with unprecedented time resolution. The paper is organised as follows: details of the experimental apparatus and its position relative to other diagnostics are provided in Section 2, the experimental scenarios of interest are presented in Section 3, resulting qualitative and quantitative considerations from the experimental data from the Cherenkov diagnostics and correlations with other diagnostics are discussed in Section 4, and considerations on Cherenkov signal profiles and a preliminary investigation into the capability of the Cherenkov probe to detect fast, kinetic perturbations involving RE losses are discussed in Section 5; conclusions are summarised in Section 6.

2. Experimental apparatus

The Cherenkov probe consists of a diamond radiator mounted on a TZM (99% Mo, 0.5% Ti, 0.1% Zr) head inserted in the FTU vessel, [6]. The synthetic, single-crystal diamond (10 mm diameter, 1 mm thickness) exposed to the plasma, Figure 1, is coated with a 100/200/1000 nm Ti/Pt/Au interlayer with the dual function of permitting possible future depositions of Mo layers to increase the electron energy threshold, and to filter out visible light, particularly the plasma D_α line. The electron energy threshold of the diagnostics is 58 keV, when including both the diamond refractive index and the effect of the Ti/Pt/Au coating. From Figure 1, showing a picture of the diamond window that was exposed to the plasma taken during the shut-down period after the experimental campaigns of interest, it is noted that during the various exposures to plasma the probe was progressively partially coated by a thin film of Mo resulting from local melting and re-deposition, resulting in a possible slight increase in the energy threshold. However, the energy threshold increase is thought to be small considering that a Mo-layer of 160 μm is necessary to increase the threshold to 360 keV only. Cherenkov radiation emitted within the diamond is coupled to a high-OH VIS/UV optical fibre connected to a high-gain photomultiplier tube (Hamamatsu R2059, 160-650 nm, 2 ns response time, 2 kV, 3×10^6 gain; and later Hamamatsu R374: 185-850 nm, 15 ns response time, 1.4 kV supply voltage corresponding to 6×10^6 gain). The readout resistor was set to R = 1kΩ to achieve simultaneously best dynamic range and amplification. The data acquisition rate was 2 MHz over the duration of the discharge (up to 2s), thus resulting in a high temporal resolution of 1 μs, comparable to or better than that of other relevant diagnostics available in FTU.

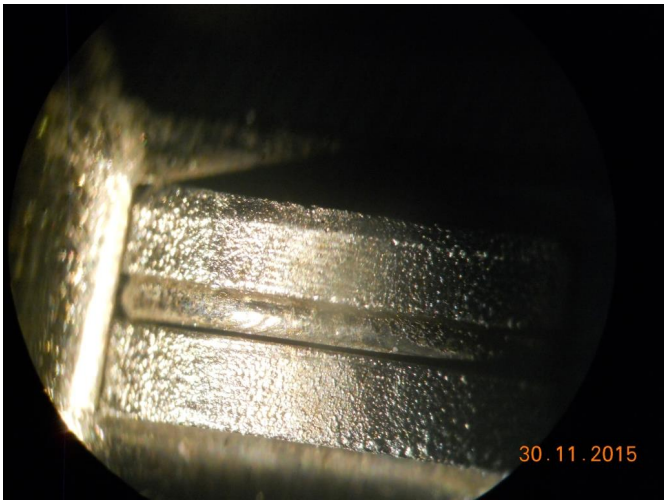

Figure 1: Picture of the probe entrance slit taken during the shut-down following the experimental campaigns of interest in this paper, showing the probe in good order.

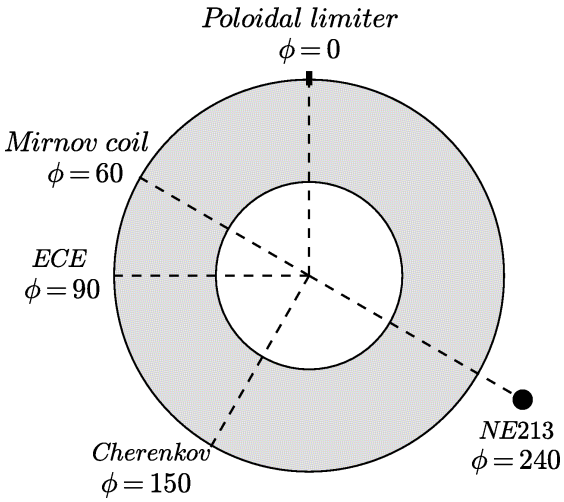

Figure 2: Top view schematic of the equatorial section of FTU with positions of relevant diagnostics. Mirnov coils are arranged at different poloidal and toroidal locations to resolve MHD mode numbers; the equatorial one used for time correlations is shown here. Plasma current is counter-clockwise; mode rotation is clockwise.

FTU is a compact, high field (up to B = 8 T) tokamak, with major radius R_0 = 0.935 m and wall radius a = 0.33 m, comprising toroidal and poloidal limiters; the former on the high field side, and the latter formed by an 86 deg segment placed at the low field side, at 29-30 cm from R_0 (the smaller distance used in pulses with large RE content in order to reinforce wall protection). Deuterium discharges are analysed here, with typical plasma parameters ranges: I_p = 0.3-0.5 MA plasma current, B = 4-5.3 T toroidal magnetic field and n_e = 0.1-1 × 10^{20} m^{-3} line-averaged density. The Cherenkov probe was positioned on the equatorial plane at ϕ = 150 deg from the poloidal limiter, Figure 2, at a radial position r = 0.310-0.320 m, in the limiter shadow. The detector head

was positioned inside the FTU vessel with the long side of the slit (0.1 cm × 1.2 cm) parallel to the equatorial plane of the tokamak.

The scenarios presented in this paper have been analysed using data from the following diagnostics: neutron and gamma ray detectors, Mirnov coils and Electron Cyclotron Emission (ECE). The diagnostics, [7], are briefly described in the following paragraphs, and their relative positions in FTU are presented in Figure 2.

A liquid organic proton recoil scintillator (NE213) (10 cm diameter × 5 cm thickness, operated in current mode with 20 kHz sampling rate) and six proportional counters (BF3) are used to monitor gamma and neutron emissions, [8]. The NE213 scintillator is located outside the magnet structure, on the equatorial plane, at ϕ = 240 deg, and is sensitive to both neutron and gamma rays. Six absolutely calibrated BF3 proportional counters (5 ms acquisition time, not sensitive to gamma rays) placed above the tokamak are used to monitor the neutron yield. The two types of detectors, NE213 and BF3, are cross-calibrated such that their outputs are identical in the absence of gamma rays, when signals from both diagnostics are due only to 2.45 MeV neutrons from D-D reactions. In the presence of REs, the scintillator, NE213, measures also gamma rays produced by REs interacting with the plasma itself, and with plasma facing components: the gamma ray contribution can, thus, be obtained by subtracting the neutron baseline (BF3) from the NE213 signal.

The plasma magnetic activity is monitored by means of a set of Mirnov pick-up coils aligned to measure the poloidal field component. The poloidal (m) and toroidal (n) periodicity numbers of perturbations are determined by cross-phase measurements. Relevant mode numbers in the following are m=2, n=1. In the presence of a magnetic island, pick-up coils facing the island O-point detect poloidal field minima. Mode amplitude and O-point location are monitored by an equatorial pick-up coil at 60 deg toroidal distance from the poloidal limiter and -90 deg distance from the Cherenkov probe, having defined increasing angles in the counterclokwise direction as seen from above the equatorial plane (Figure 2). The coil voltage is multiplied by the effective area and integrated to obtain the poloidal field. Maxima and minima are detected and combined to form the relative amplitude (in percent) $\delta B/B = 100 \times (B_{max}-B_{min})/(B_{max}+B_{min})$. Times of maxima and minima are used in the following to define intervals for comparison with other diagnostics. The relative amplitude can be used as a boundary condition for the linear tearing mode eigenfunction to roughly estimate the island width under the simplifying assumptions of cylindrical geometry and small island.

Further information on the internal mode structure, in particular the presence of an $m = 1$, $n = 1$ toroidal sideband, is obtained in some cases from temperature profile oscillations measured by a fast multichannel electron cyclotron emission (ECE) diagnostics. The ECE sightline is located on the equatorial plane, at 90 deg toroidal distance from the poloidal limiter and -60 deg distance from

the Cherenkov probe (Figure 2). The available channels do not encompass the island, but permit to evaluate the plasma displacement by the tearing mode in a region enclosed by the island chain radius. Full ECE spectra, which are available with 5 ms time resolution, permit monitoring the presence of non-thermal emission by runaway electrons.

3. Experimental scenarios

The signal traces for this study have been obtained from experiments dedicated to REs and MHD instabilities control in FTU (experimental campaigns 2013-C2, 2014-C2 and 2015-C1). Three scenarios are analysed in this paper, characterised by different RE generation conditions and in particular by different values of the Dreicer field (E_D), and of the Connor-Hastie relativistic critical field (E_c) [9]:

i. *Type 1 Medium density scenario*: pulses designed for experiments on MHD control by ECRH, with MHD activity induced by mild Neon injection on medium-density plasmas (about a factor two below the density limit) with toroidal field B_t = 5.3 T and plasma current I_p = 0.5 MA. Typical line average densities were 6×10^{19} m^{-3} before Ne injection and 8×10^{19} m^{-3} before disruption, Figure 3. The development of MHD activity was slow for hundreds of milliseconds and then changed to rapid (5 ms typical) growth and locking, followed by disruption. The toroidal electric field was approximately 0.2-0.35 V/m, corresponding to 1-2% of E_D and to 2-5 times E_c (Table 1). The RE population was mainly generated in the early stages of the discharge. The gamma-ray count rates at the beginning of the disruptive phase ranged from 0.28×10^{12} s^{-1} to 4.1×10^{12} s^{-1}, and increased by at least one order of magnitude during the final MHD growth;

ii. *Type 2 Low density scenario*: pulses designed to induce post-disruption RE plateaus by strong injection of Neon or Argon in low-density ($3\text{-}4 \times 10^{19}$ m^{-2}) plasmas at B_t = 4.0 T, I_p = 0.5 MA, with the (2,1) mode developing even before the programmed gas injection. MHD activity increased quickly after impurity injection. The toroidal electric field was approximately 0.4 V/m, corresponding to 3-5% E_D and to 8-10 times E_c. Considering the typical avalanche threshold, $E/E_c \approx 4$ found in FTU, [10], Table 1, in such pulses, REs were generated continuously and the gamma-ray count rate increased exponentially before the disruptive phase, Figure 4;

iii. *Type 3 RE generation in very low density plasma scenario*: pulses at very low density 1.5×10^{19} m^{-2}, B_t = 4.0 T, I_p = 0.36 MA, with the 2/1 mode developing spontaneously before Ar injection at t = 0.6 s, Figure 5. The toroidal electric field was approximately 0.3 V/m, corresponding to 6% E_D and to 17 times E_c. The gamma count rate increased exponentially to 2.3×10^{13} s^{-1}, before the onset of instabilities.

In pulses of type 1 with higher gamma-ray count rates, e.g., 37607, ECE spectra during RE initial formation feature a peak below the second harmonic and a weak continuum, showing evidence of synchrotron emission by REs, Figure 6. However, suprathermal features disappear before the disruptive phase and fast ECE measurements can then be confidently used to infer the internal mode structure evolution during the disruptive phase. This aspect will be discussed in more detail in the following Sections. By contrast, ECE spectra in Type 3 pulses (lower frame in Figure 6) are dominated by suprathermal emission; the latter can be exploited to obtain information on RE dynamics as discussed in Section 5.

In the following Sections, results from the above scenarios will be presented to analyse the information that can be extracted from the Cherenkov probe in pre-disruption scenarios and correlations between diagnostics, Section 4; and the characteristic features of the signal profiles detected by the Cherenkov probe, with a preliminary investigation into its capability to detect fast, kinetic perturbations involving RE losses, in Section 5.

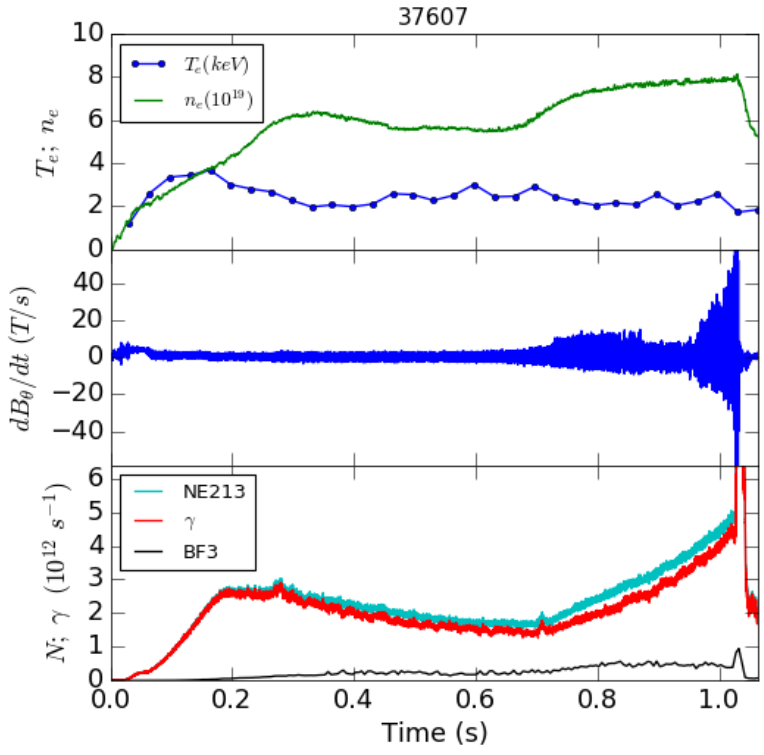

Figure 3: Time-evolution of plasma parameters for type 1 pulses (FTU pulse #37607 B = 5.3 T, I = 0.52 MA, 50 ms Ne puff at 0.5 s). Plasma parameters are, from the top panel: plasma line-averaged density from interferometry and electron temperature from Thomson scattering, Mirnov coils amplitude signal (reference channel 26), and NE213 (cyan), BF3 (black) and gamma (red) signals. Magnetic and gamma signals are out of scale during disruption.

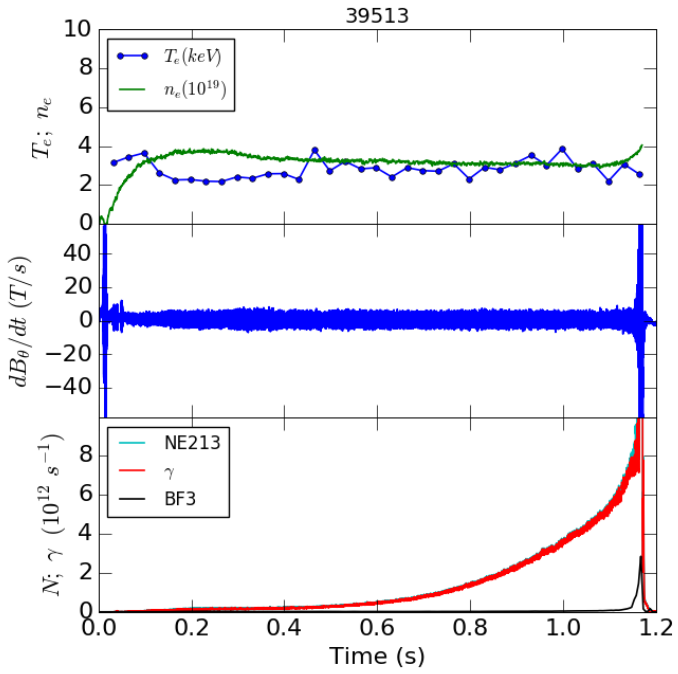

Figure 4: Time-evolution of plasma parameters for type 2 pulses (FTU pulse #39513 B = 4.0 T, I = 0.5 MA, 30 ms Ar puff at 1 s). Plasma parameters are, from the top panel: plasma line-averaged density from interferometry and electron temperature from Thomson scattering, Mirnov coils amplitude signal (channel 26), and NE213 (cyan), BF3 (black) and gamma (red) signals. Magnetic and gamma signals are out of scale during disruption.

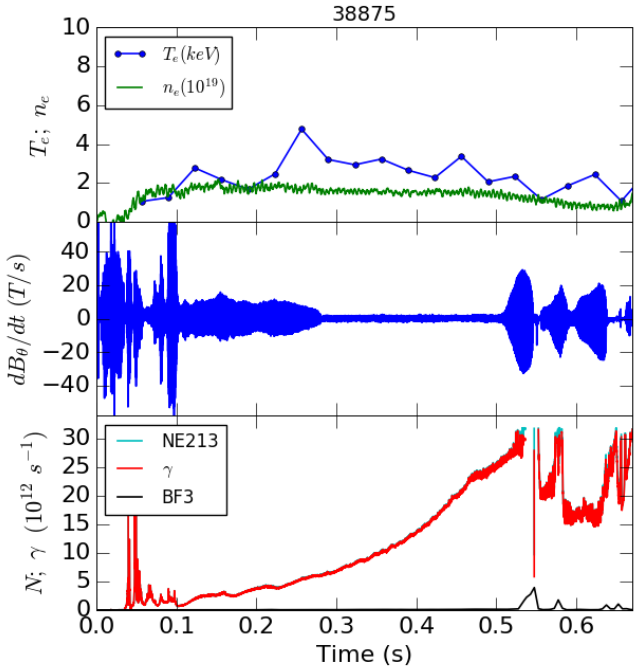

Figure 5: Time-evolution of plasma parameters for type 3 pulses RE generation in very low density plasma scenario (FTU pulse #38875 B = 4.0 T, I = 0.36 MA, 50 ms Ar puff at 0.6 s). Plasma parameters are, from the top panel: plasma line-averaged density from interferometry and electron temperature

from Thomson scattering, Mirnov coils amplitude signal (channel 26), and NE213 (cyan), BF3 (black) and gamma (red) signals.

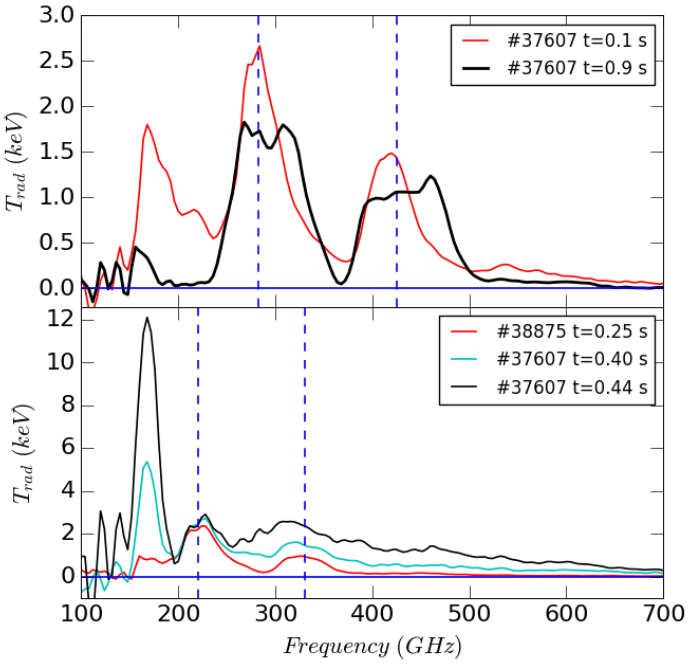

Figure 6: ECE spectra evolution in Type 1 (upper frame) and Type 3 (lower frame) discharges. Dashed lines show frequencies of second and third harmonics of the electron cyclotron frequency at the plasma center. The black line in the upper frame shows a typical thermal spectrum. Emission at frequencies below160 GHz is blocked by a filter used to reject stray ECRH power.

Table 1: List of pulse characteristics for the scenarios of interest at time t, including toroidal field B, plasma current I_p; E, E_c and E_D inductive, critical and Dreicer electric field, respectively; gamma count rate; average density; Cherenkov probe distance from the projected limiter position.

Pulse #	B (T)	Ip (MA)	t (s)	E (V/m)	E_c (V/m)	E_D (V/m)	Gamma counts ($\times 10^{12}$ s^{-1})	n_{AV} ($\times 10^{19}$ m^{-3})	Cherenkov probe distance (cm)
37606	5.3	0.5	**0.9**	0.31	0.1	26	0.45	8.4	1.5
37607	5.3	0.5	**1.0**	0.35	0.096	30	4.1	7.8	1.5
37608	5.3	0.5	**0.9**	0.32	0.1	27	0.28	8.3	1.5
37609	5.3	0.5	**0.75**	0.34	0.1	29	4.0	8.6	1.5
39513	4.0	0.5	**1.1**	0.39	0.04	8	5.3	3.0	2.0
39593	4.0	0.5	**0.75**	0.4	0.051	12	3.2	4.2	2.0
38875	4.0	0.36	**0.5**	0.3	0.018	5	25	1.2	2.0

4. RE expulsion by disruptive tearing modes

RE losses during the tearing mode growth in the disruption precursor phase of scenarios 1 and 2 occur on a time scale that is much shorter than the RE production timescale. On the other hand, the time scale is sufficiently long to resolve several rotation periods of the magnetic island, which provide a natural signal modulation. These scenarios are therefore particularly useful to study the dynamics of non-thermal electrons and to identify key interaction mechanisms of REs with magnetic perturbations.

4.1 Time evolution during the disruption precursor

In the disruptive phase of type 1 and type 2 pulses, the MHD amplitude evolution suddenly changes from slow to rapid (disruption precursor). The magnetic perturbation in terms of percent deviation from the equilibrium poloidal field at the sensor ($\delta B_{pol}/B_{pol}$) typically increases from 0.05% to 1.5% in 5 ms and then locks. The disruption thermal quench follows locking after 1-50 ms. The evolution of Cherenkov probe signal, magnetic perturbation amplitude and gamma-ray counts during this phase in the two types of scenarios are shown in Figures 7 and 8, respectively. Both Cherenkov signal and gamma-ray counts dramatically increase during mode growth, an evidence of enhanced RE expulsion. Furthermore, both signals are modulated at the island rotation frequency, showing that RE expulsion is non-axisymmetric. It is important to note that the Cherenkov signal is at the noise level before mode growth.

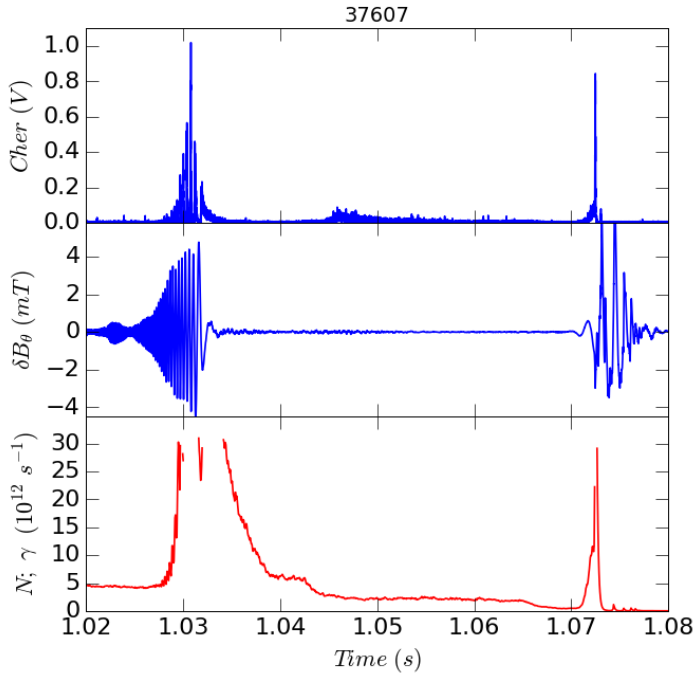

Figure 7: Evolution of disrupting event in type 1 pulses medium density scenario (FTU pulse #37607 B = 5.3 T, I = 0.52 MA, 50 ms Ne puff at 0.5 s, 100 ms ECRH at 0.7 s): Cherenkov probe signal, magnetic perturbation and gamma-ray counts (not shown when saturated).

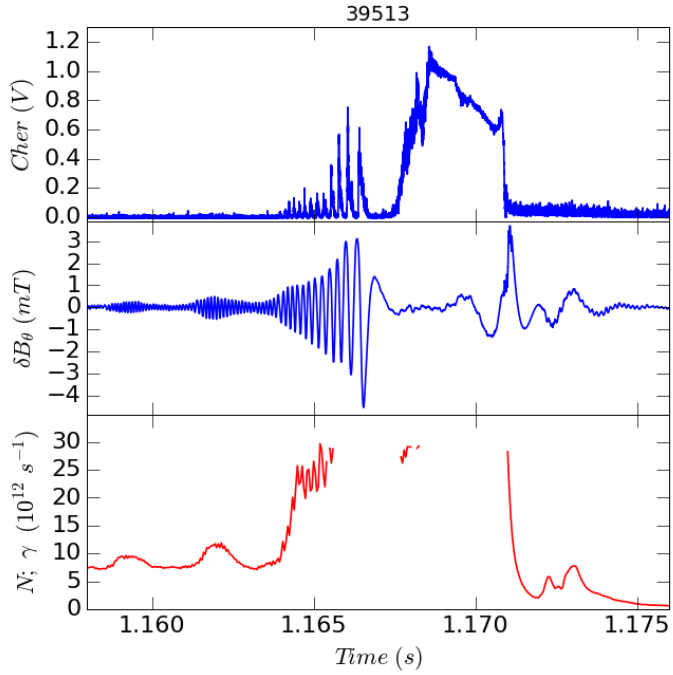

Figure 8: Evolution of disrupting event in type 2 pulses low density scenario (FTU pulse #39513 B = 4.0 T, I = 0.5 MA, 30 ms Ar puff at 1 s): Cherenkov probe signal, magnetic perturbation and gamma-ray counts (not shown when saturated).

In pulses from scenario 1, a RE population is produced in the early stages of the discharge because of the low initial density of the plasma. Evidence of the presence of a RE population is in the separation between the NE213 and BF3 time traces, Figure 3. In such pulses, gamma ray emission rates quickly increase in the initial part of the pulse ($t < 0.2$ s); subsequently decreasing until Ne injection, and then showing a progressive recovery (by a factor of up to 3, approximately, but much less in other pulses of the same type), before culminating in strong fluxes at disruption. Depending on conditions at $t < 0.2$ s, count rates at the end of the current flat top range from 0.28×10^{12} s^{-1} to 4.1×10^{12} s^{-1}, Table 1; in all cases, count rates increase by at least one order of magnitude during the final 2/1 mode growth. In this phase, the 2/1 mode is coupled to a central 1/1 component, a mechanism that can enhance RE expulsion by magnetic perturbation because of the juxtaposition of deformations with different helicity. The 1/1 component is revealed by odd-parity temperature oscillations around the plasma centre that are synchronous with 2/1 magnetic oscillations.

A more accurate analysis in terms of phase lags using the magnetic signal as a clock is shown in Figure 9. O-point passages at the Mirnov coil port are identified from magnetic signal minima. Times of O-point passages at other toroidal locations are estimated by time-shifts proportional to the oscillation period and to the normalised toroidal distance. Electron temperature oscillations

measured close to the internal side of the island have minima at the estimated O-point passages, as expected [11].

Expelled REs are detected by the Cherenkov probe, when the O-point of the magnetic island is close to facing the probe location. On the other hand, the gamma ray signal shows maxima shortly after the O-point passage at the poloidal limiter port. A nearly anti-phase correlation between Cherenkov and gamma signals was noted in [6] and attributed to the fact that the gamma signal is produced by REs preferentially interacting with the poloidal limiter, which is at 150 deg toroidal distance from the Cherenkov probe.

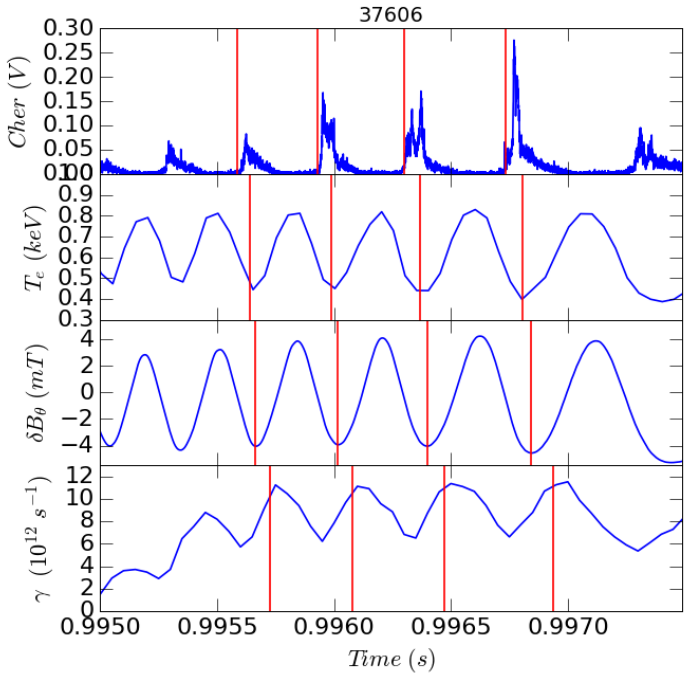

Figure 9: Modulation and relative timing of Cherenkov and gamma ray signals during island rotation, growth and locking in type 1 scenario (FTU pulse #37607 B = 5.3 T, I = 0.52 MA): Cherenkov probe signal, ECE electron temperature at a location close to the q=2 radius, magnetic perturbation amplitude and gamma-ray counts. Estimated O-point passages at the respective ports are shown by vertical bars (the poloidal limiter port and not the NE213 location is considered for gamma-ray counts). A pulse with low pre-disruption gamma count rate was selected to avoid saturation of the NE213 signal.

Two distinct features characterise Cherenkov and gamma ray signals. The first and most evident aspect is that the Cherenkov signal returns to zero after the passage of the O-point near the probe (100% contrast), indicating a strongly non axisymmetric flux of escaping REs in the limiter shadow where the probe is located. Also gamma counts present a modulation, although much softer (< 25% contrast).

The second distinguishing characteristics is that the Cherenkov peaks are non-symmetric, rising rapidly and decaying slowly. As an example, the time evolution of the shape of the peaks detected during the disruption precursor in a type 1 pulse, is presented in Figure 10, where the Cherenkov signal is plotted against a normalised time defined as $phase = (t - t_X)/(t_O - t_X)$, where t_X and t_O are the time of, respectively, the minimum and maximum of the amplitude of the magnetic perturbation, indicating the passage of the X and O points in front of the reference Mirnov coil. A most notable feature in Figure 10, is that multiple sub-peaks progressively develop while the tails remain in overlap. Typical FWHM (full-width at half maximum) of the sub-peaks is 20-30 μs. Each period reveals an increasingly complex RE emission structure, which reflects the interplay between island structure, RE diffusion during island rotation and the geometry of obstacles in the vessel. A similar picture arises from scenario 2, Figure 11, although here the peak structure is more complex, featuring a different sub-peaks structure, likely due to the different RE acceleration regime. From Figures 10 and 11, it is noted that the peak duration is approximately the same in the two cases. The amplitude of the peaks depends on several factors, as discussed in more detail in Section 4.2.

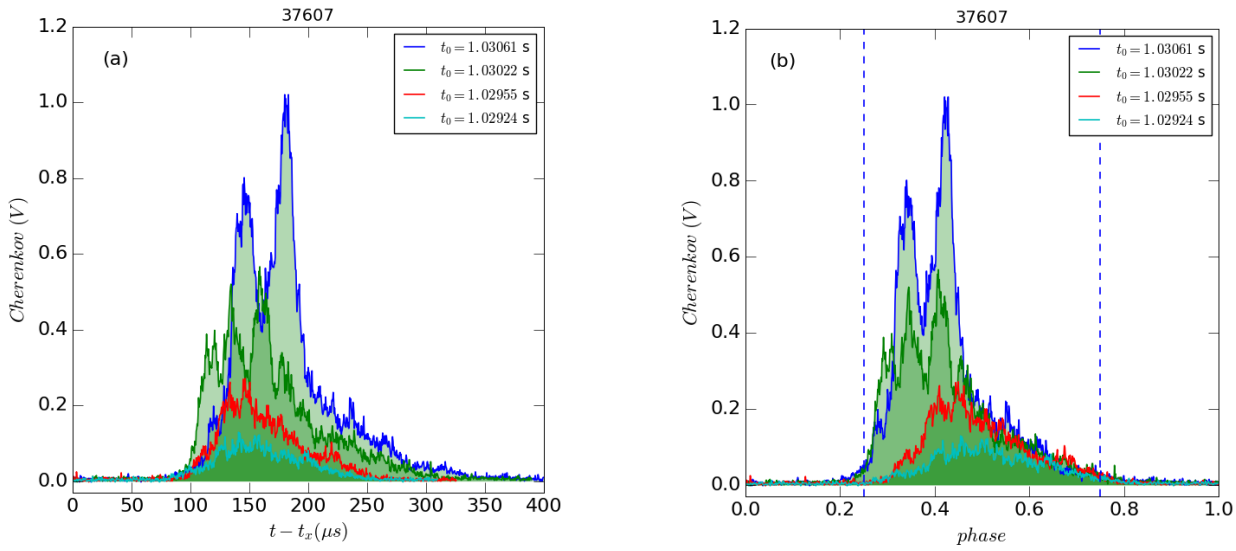

Figure 10: Time evolution of Cherenkov peaks profiles for type 1 FTU pulse 37607 during each magnetic oscillation period: intensity as a function of (a) time delay t-t_x, and (b) phase, where the vertical line at 0.25 indicates the O-point passage at the probe port, while the one at 0.75 shows the X-point passage. Clearly visible are the increasing complexity of the peaks, and the subsequent overlapped tails.

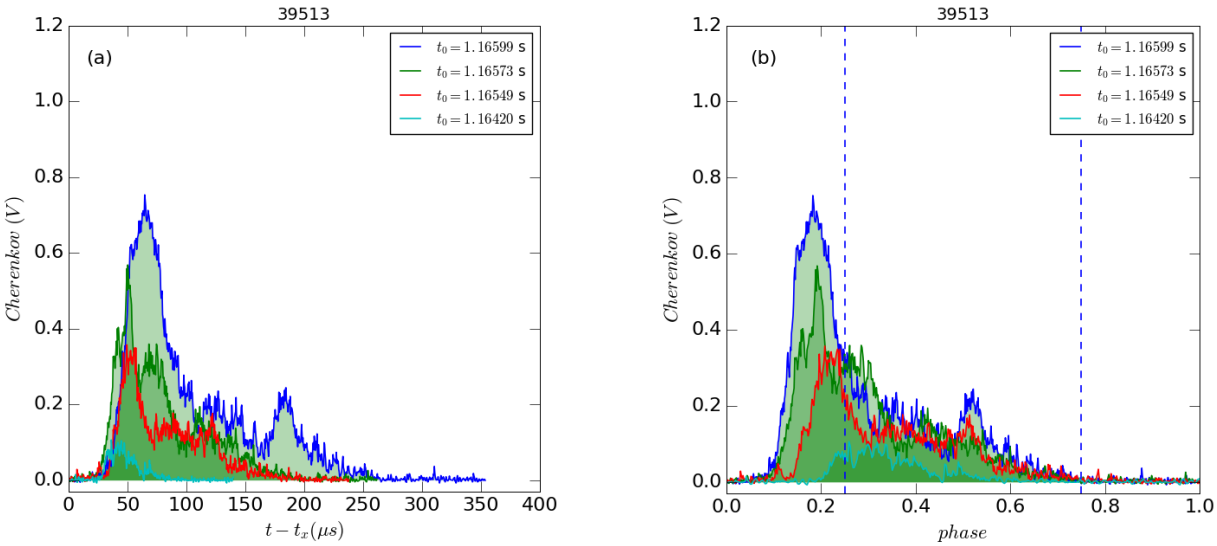

Figure 11: Time evolution of Cherenkov peaks profiles for type 2 FTU pulse 39513: intensity as a function of (a) time delay t-tx, and (b) phase.

4.2 Quantitative considerations on the Cherenkov signal: correlation with gamma ray counts and with magnitude of magnetic perturbation

The Cherenkov probe is an integrated diagnostics where the optical signal generated in the radiator (diamond in the present case), is coupled to the detector via an optical fibre. Clear advantages of using a Cherenkov probe are a direct detection of expelled electrons, and a precise spatial localisation of the measurements. On the other hand, the Cherenkov signal carries mixed information on temporal variations of both the energy and the number of expelled runaway electrons, which may limit the interpretation capability of the corresponding experimental data. This limitation is common also to other plasma diagnostics, including for example neutron and gamma ray counters. However, it is worth deriving correlations with other diagnostics to maximise the level of information obtained about specific experimental scenarios. From the analysis of several pulses from the pre-disruption scenarios described in Section 4.1 above, it was possible to obtain a quantitative correlation between Cherenkov signal intensity and gamma ray rate on the one side, and between Cherenkov signal and magnetic perturbation on the other. Considering that the three factors are strongly coupled, it is useful to analyse first the correlation between gamma-ray counts and magnetic perturbation, then the correlation between Cherenkov signal and magnetic perturbation, and finally the correlation between Cherenkov signal and gamma-ray counts.

Gamma ray rates versus magnetic perturbation for pulses of types 1 and 2 are presented in Figure 12. The first consideration is that the plot shows several different trajectories when using raw data. On the other hand, by normalising the data with respect to the count rate just before mode growth (γ_0), a more ordered picture arises with two trajectories, one for type 1 and one for type 2 pulses. In

other words, the increasing magnetic perturbation amplifies the pre-existing gamma count rate. The maximum amplification for type 1 is a factor 80. For pulses of type 2 maximum values are smaller (<5), but the amplification is steeper and values at the same magnetic amplitude are larger than those obtained for type 1 pulses.

Cherenkov signals versus magnetic perturbation are shown in Figure 13. Trajectories of type 2 pulses are significantly higher and steeper than those corresponding to type 1 pulses, with similar levels of magnetic perturbation. The photomultiplier tube was changed during the experimental campaign (from Hamamatsu R2059: 160-650 nm, 2 kV supply voltage corresponding to 3×10^6 gain; to Hamamatsu R374: 185-850 nm, 1.4 kV supply voltage corresponding to 6×10^6 gain after pulse 39485); therefore, the comparison is only qualitative, but the different shape of emission rates between scenarios is valid. This difference cannot be explained in terms of island width. The full island width as estimated using the tearing mode eigenfunction for a pulse of type 1 is 3 cm at $(\delta B/B) \sim 0.1$ %; estimates for larger perturbations are meaningless as the small island approximation fails. No such estimate is available for type 2 pulses, the quality of diagnostic data being insufficient to calculate eigenfunctions. However, since the edge safety factor for type 2 is smaller and then the q = 2 radius is closer to the Mirnov coil than in type 1 pulses, the island width at the same perturbation amplitude should be smaller for pulses of type 2 than that obtained for type 1 pulses. The reason for the different responses is most likely that RE generation in type 2 pulses is continuous, compared to the RE generation occurring mainly in the initial stages of type 1 pulses (Figures 3 and 4), implying that the two types of pulses are characterised by different RE distributions, as already indicated by the different pulse shapes in Figures 10 and 11.

When correlating the Cherenkov signal with the gamma-ray counts, Figure 14(a), roughly linear trajectories are obtained, but with different slopes for different pulses. In fact, whereas the Cherenkov signal with small magnetic perturbation is at the noise level, the gamma-ray counts base level differs from pulse to pulse; the trends converge to the same point only when the magnetic perturbation becomes significant. Plotting the Cherenkov data against magnetic perturbation combined with gamma-ray counts, a neater linear trend is visible, Figure 14(b), showing a linear correlation between parameters when the Cherenkov signal emerges from noise.

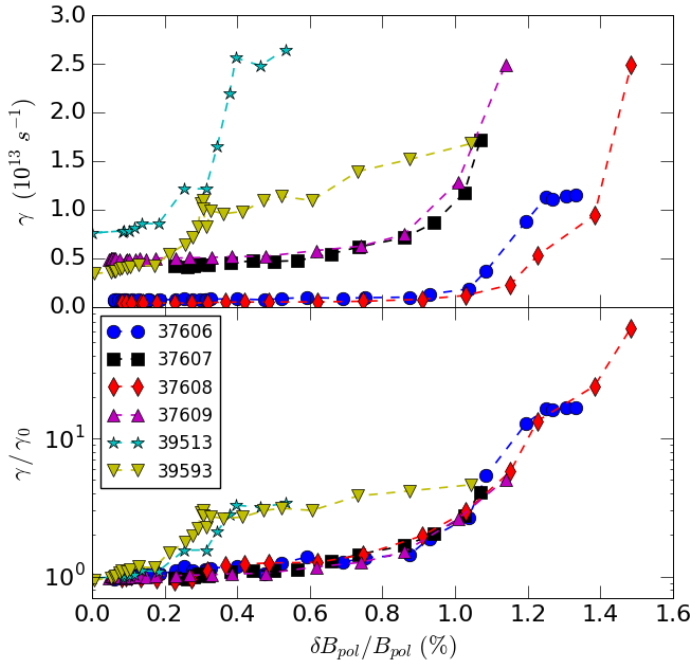

Figure 12: Correlation between gamma-ray counts (top) and gamma-ray counts normalised to the initial level (lower panel) with relative magnetic perturbation amplitude. [Lower plot in semi-log scale.] Trajectories of pulses 37607, 37609 and 39513 are truncated because of the saturation of NE213 detector.

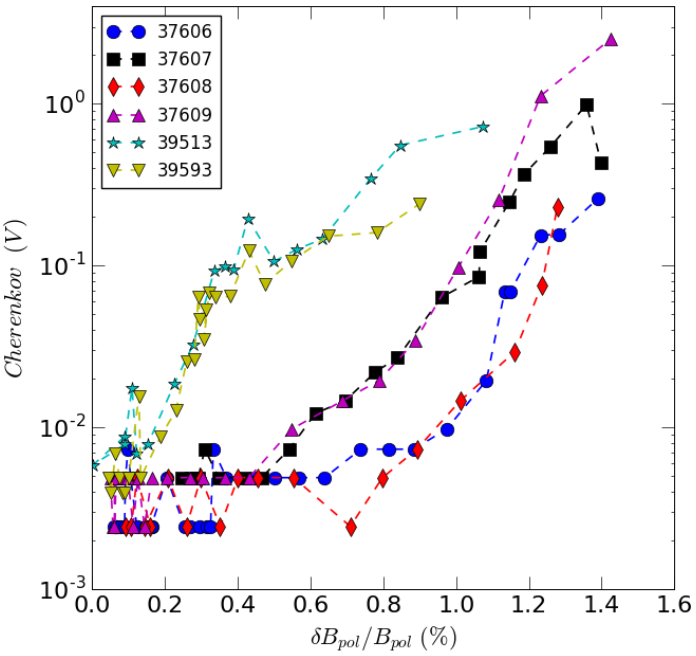

Figure 13: Correlation between Cherenkov signal and magnetic perturbation.

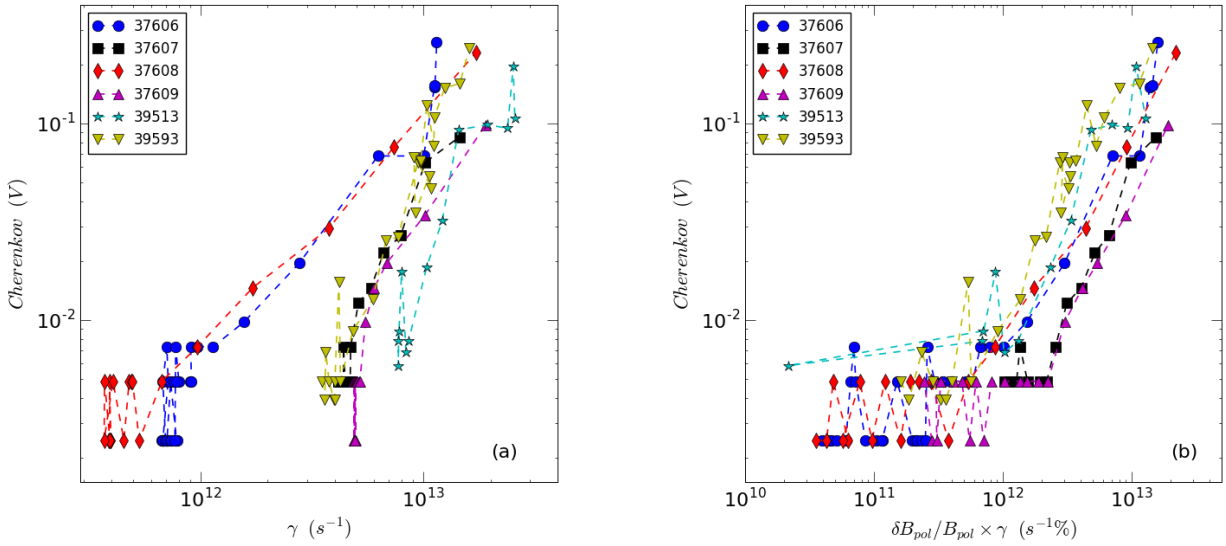

Figure 14: Correlation between Cherenkov signal and (a) gamma-ray counts, and (b) magnetic perturbation combined with gamma-ray counts.

5. Evidence of fast RE expulsion by kinetic instabilities

Scenarios developing kinetic instabilities present particularly interesting Cherenkov signal traces where RE expulsion events characterised by different time scales can be identified. The attention is focussed here on pulses that present the coexistence of two profoundly different instabilities, one of the MHD type – the tearing mode; the other a fast kinetic instability, both detected with a high level of detail by the Cherenkov probe. Type 3 pulses were designed to achieve RE generation at very low plasma density, $n_{lin} = 1.5 \times 10^{19}$ m^{-2}, B = 4 T, $I_p = 0.36$ MA. In such conditions, the (2,1) mode developed even before the 50 ms Ar injection programmed at t = 0.6 s. Hence, the events of interest occur before Ar injection. The toroidal electric field was about 0.3 V/m, corresponding to 6% E_D and to 17 times E_c, implying a continuous RE generation rate during the pulse, and a corresponding exponential increase of the gamma ray count rate to a very high level of 2.3×10^{13} s^{-1}, before the onset of instabilities.

In this scenario the Cherenkov signal presents two superimposed signatures, one due to the magnetic island as discussed so far, the other due to another type of instability growing on a much shorter time scale, Figure 15. The short time scale, characterised by a Cherenkov response rise time of the order of the microsecond makes it possible to categorise it as a kinetic instability. A succession of four such events with sharp rise and slower decay is visible in Figure 15 before t = 0.53 s; further events occur later, superimposed to the slowly evolving envelope of oscillations due to the tearing mode. The first instance of the fast instability was detected by the Cherenkov probe at 0.39 s.

Signs of this fast instability are picked up also by both gamma ray detector and ECE, which in this case is dominated by suprathermal emission (Figure 6). Both signals suddenly increase at each event, and then decay with different time scales. The kinetic events occur at irregular intervals – there does not seem to be a clear periodicity associated to this event.

While the sharply increasing Cherenkov signal can be explained by the sudden enhancement of RE losses, the simultaneous increase of the ECE signal can only be due to a sudden increase of RE perpendicular momentum. A well known mechanism that can justify this observation is the anomalous Doppler (or fan) instability [12]. Because of its better time resolution, the Cherenkov probe provides unique information on the rise time of the instability, measured here with unprecedented time resolution, which varies from a few microseconds in the earlier events, to < 1 μs (limited by the sampling time in this instance), in the later ones toward the end of the instability.

The effect of the magnetic activity is different from the one reported in Section 4, in connection with disruption precursor tearing modes. At first, the Cherenkov signal presents the two types of peak response characterised by the slow (tearing mode) and fast (kinetic instability) timescales each with a specific, constant amplitude, Figure 16(a). Then, the amplitude of both types of peaks increases at nearly constant magnetic amplitude, but with the peaks corresponding to the tearing mode showing a much more dramatic amplitude increase and modulation (Figure 15), while at the same time the gamma signal saturates. At this stage, the Cherenkov probe signal peaks differ from those observed in correspondence with the disruption precursor for having a different phase-shift with respect to the magnetic signal. It is remarkable that in this situation, the Cherenkov signal shape versus phase changes dramatically during amplitude growth, as shown in Figure 16: shapes at low amplitude are at the noise level around phase=0 and phase=1, Figure 16(a), such as in Figures 10-11, whereas shapes at high amplitude have maxima at such phase values, Figure 16(b). Although conditions are very different, with more copious RE production and slower mode growth in type 3 pulses, the striking difference of shapes indicates that different kinds of interaction with magnetic perturbations can be present. A possible explanation is that the peaks shape changes when a significant population of trapped energetic electrons forms due to a cumulative effect of anomalous Doppler instability events. The presence of a cumulative effect is consistent with the continuous rise of ECE traces in Figure 15. After the Ar puff the system becomes irreversibly unstable and the RE beam confinement is lost over a period of approximately 200 ms, leading to plasma disruption and termination, Figure 17. The final RE loss is intercepted by the Cherenkov probe, resulting in a signal that does not return to zero until plasma termination, Figure 17.

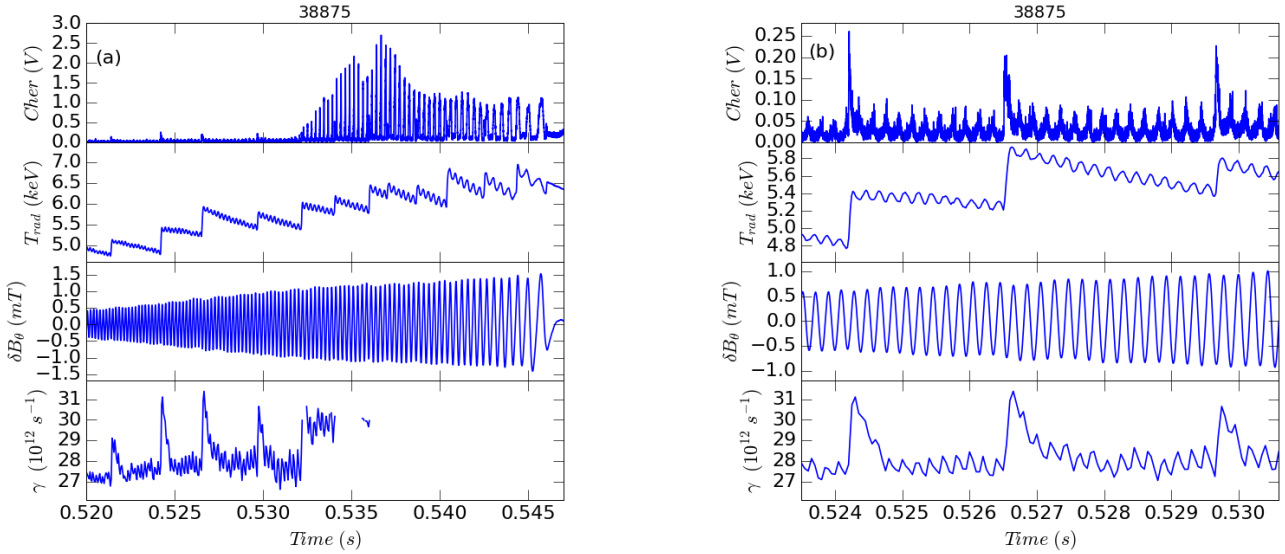

Figure 15: Type 3 scenario at very low density (FTU pulse #38875 B = 4.0 T, I = 0.36 MA, 50 ms Ar puff at 0.6 s): (a) Cherenkov, ECE signal at 350 GHz, a frequency with nearly zero thermal emission, Mirnov coils amplitude signal (channel 26), and gamma time traces; and (b) expanded view with three events superposed with the slow modulation due to the rotating MHD. The gamma ray trace is not shown when the NE213 detector saturates. The ECE radiation temperature is well above the thermal level (< 3 keV from Thomson scattering), showing RE dominated emission.

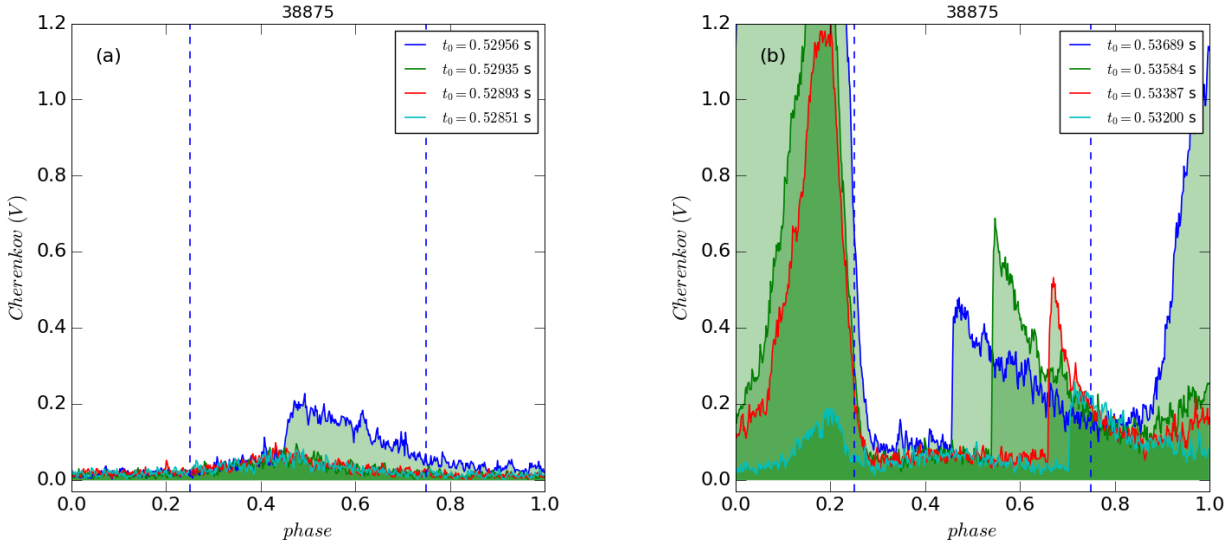

Figure 16: Time evolution of Cherenkov peaks profiles as a function of the phase, for type 3 FTU pulse 38875 during each magnetic oscillation period: (a) evidence of fast raise time of the peak corresponding to the fast instability, superposed with broader peaks corresponding to MHD-driven RE losses following the passage of the O-pint in front of the probe (vertical line at 0.25 phase); (b) evolution of the pulse showing an increase in amplitude in both types of losses, while the MHD-driven losses become phase-shifted; toward the end of the sequence of

events, when the MHD mode locks, the amplitudes reduce for both types of peaks, until the detected signal is levelled.

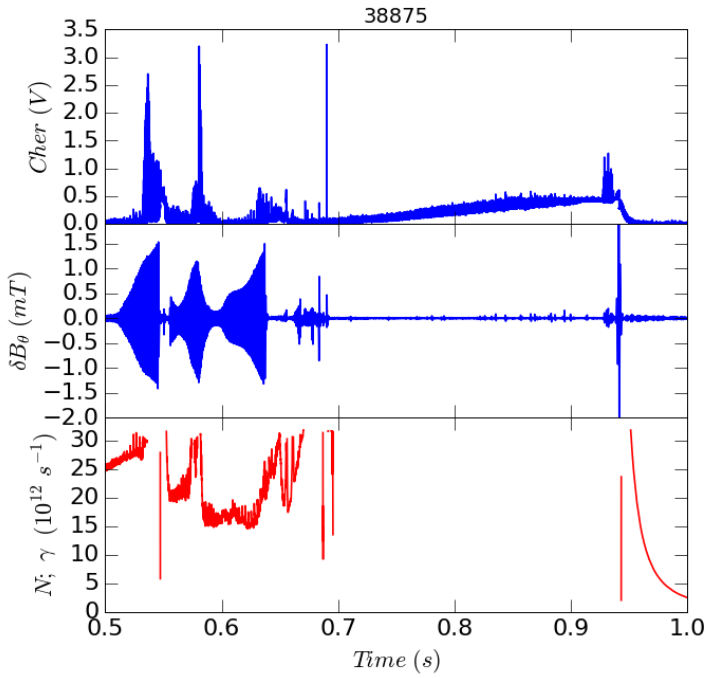

Figure 17: Type 3 pulses final RE loss intercepted by the Cherenkov probe, resulting in a signal that does not return to zero until plasma termination. From the top: Cherenkov signal, magnetic perturbation amplitude, gamma-ray count rate (not shown when saturated).

Conclusion

Three scenarios were analysed, characterised by different RE generation rates and mechanisms. RE expulsion by two different kinds of instabilities were studied in those scenarios, the tearing mode and the anomalous Doppler instability. The main observations from experiments involving tearing modes in the disruption precursor phase (with amplitude growing on time scales much shorter than RE generation times) can be summarised as follows:

1. The Cherenkov signal is characterised by peaks which repeat as the tearing mode rotates, featuring a 100% contrast, i.e., the signal returns to the noise level during some phase intervals of mode rotation; this implies that RE expulsion is strongly asymmetric.
2. The gamma-ray emission trace is modulated as well, but with a soft contrast, typically < 25%;
3. The Cherenkov signal peaks appear roughly aligned when plotted against the phase of MHD rotation cycles;
4. Cherenkov peaks are asymmetric, with sharper leading edge followed by tails; the leading edge features sub-peaks;

5. The correlation between gamma-ray emission and magnetic amplitude shows an amplification of the initial emission which is the same for each scenario, but presents different shapes for different scenarios;
6. The correlation between the Cherenkov signal and the magnetic amplitude multiplied by the gamma-ray rate presents a good alignment;
7. RE expulsion by the disruption precursor is incomplete, in fact significant peaks of Cherenkov and gamma-ray signals are observed in the final stages of the disruption.

The main observations from experiments at very low density involving a substantial RE population can be summarised as follows:

1. The Cherenkov probe signal presents evidence of the Anomalous Doppler instability in the form of sudden events reappearing aperiodically;
2. The growth time of RE expulsion by this instability has been measured with unprecedented time resolution;
3. In this situation the Cherenkov probe signal responds to slowly growing tearing modes with deeply modulated peaks, that can differ from those observed in correspondence with the disruption precursor for having a different phase-shift with respect to the magnetic signal.

Acknowledgement

The authors wish to acknowledge M. Rabinski, M. J. Sadowski and J. Zebrowski of the National Centre for Nuclear Research (Otwock, Poland) for the Cherenkov probe hardware. The photo in Figure 1 was taken from the FTU Technical Pool archive.

References

1. M. Lehnen et al., Disruptions in ITER and strategies for their control and mitigation, 2015 Journal of Nuclear Materials 463 39
2. T. C. Hender et al 2007 Nucl. Fusion 47 S128
3. R. J. Zhou et al., Effect of magnetic fluctuations on the confinement and dynamics of runaway electrons in the HT-7 tokamak, Physics of Plasmas 20 (2013) 032511; Ivanov et al., Interdependence of Magnetic Islands, Halo Current and Runaways Electrons in T-10 Tokamak, IAEA-CN-77/EXP2/02 Sorrento, 2000
4. M. G. Aartsen et al., The IceCube Neutrino Observatory: Instrumentation and Online Systems, JINST 12 P03012 (2017)
5. M. Rabinski *et al* 2017 *JINST* **12** C10014

6. F. Causa *et al* 2015 *Nucl. Fusion* **55** 123021
7. O. Tudisco et al., The diagnostic systems in FTU, Fusion Sci. Technol., **45** , 402-421, chapter 8
8. B. Esposito et al, Dynamics of high energy runaway electrons in the Frascati Tokamak Upgrade, Phys. Plasmas 10 (2003) 2350
9. Connor J. W. and Hastie R. J. 1975 Nucl. Fusion 15 415
10. Martin-Solis et al 2010 Phys. Rev. Lett. 105 185002; B Esposito *et al* 2017 *Plasma Phys. Control. Fusion* **59** 014044
11. R. Fitzpatrick Phys. Plasmas 2 (1995) 825
12. V. S. Vlasenkov *et al* 1973 *Nucl. Fusion* **13** 509; V. V. Parail and O. P. Pogutse 1978 *Nucl. Fusion* **18** 303; D.A. Spong et al 2018 Phys. Rev. Lett. 120 155002